CHEMISTRY OF MATERIALS

Article

pubs.acs.org/cm

Structural, Optical, and Magnetic Properties of Highly Ordered Mesoporous MCr_2O_4 and $MCr_{2-x}Fe_xO_4$ (M = Co, Zn) Spinel Thin Films with Uniform 15 nm Diameter Pores and Tunable Nanocrystalline Domain Sizes

Christian Suchomski,[†] Christian Reitz,[†] Kirstin Brezesinski,[†] Célia Tavares de Sousa,[‡] Marcus Rohnke,[†] Ken-ichi Iimura,[§] Joao Pedro Esteves de Araujo,[‡] and Torsten Brezesinski*[,†]

[†]Institute of Physical Chemistry, Justus-Liebig-University Giessen, Heinrich-Buff Ring 58, 35392 Giessen, Germany

[‡]Departamento de Fisica, Faculdade de Ciencias, Universidade do Porto, Rua do Campo Alegre 687, 4169-007 Porto, Portugal

[§]Department of Advanced Interdisciplinary Science, Graduate School of Engineering, Utsunomiya University, Yoto 7-1-2, 321-8585 Utsunomiya, Japan

Supporting Information

ABSTRACT: Herein is reported the synthesis and characterization of nanocrystalline cobalt chromite ($CoCr_2O_4$) and zinc chromite ($ZnCr_2O_4$) thin films with highly ordered cubic networks of open pores averaging 15 nm in diameter. We also show that the synthesis method employed in this work is readily extendable to solid solutions of the type $MCr_{2-x}Fe_xO_4$ (M = Co, Zn), which could pave the way for innovative device design. All of these materials can be prepared by facile coassembly of hydrated nitrate salts with an amphiphilic diblock copolymer, referred to as KLE. The as-made materials are amorphous thin films with face-centered-cubic close-packed pore structures. Electron microscopy, X-ray diffraction, grazing incidence small-angle X-ray scattering, krypton physisorption, UV−vis spectroscopy, time-of-flight secondary ion mass spectrometry, X-ray photoelectron spectroscopy, and Raman spectroscopy studies collectively verify that both the transition metal chromites and the solid solutions are well-defined at the nanoscale and the microscale. In addition, the data show that the different thin film materials are nanocrystalline after annealing in air at 600 °C, adopt the spinel structure in phase-pure form, and that the conversion of the initially amorphous frameworks comes at little cost to the ordering of the cubic pore-solid architectures. Magnetization studies as a function of temperature and field further reveal the high quality of the KLE-templated $CoCr_2O_4$ thin films with both long-range ferrimagnetic order and spiral magnetic order at low temperatures, in agreement with previous findings.

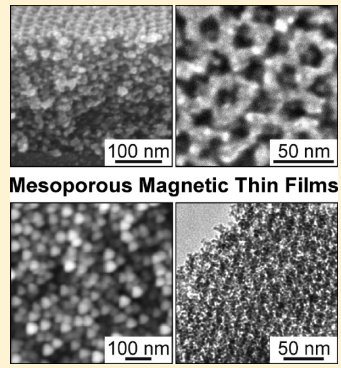

KEYWORDS: *chromite, ferrite, spinel, thin film, self-assembly, mesoporous, magnetic, multiferroic*

INTRODUCTION

Transition metal chromites with the general formula MCr_2O_4 or $MO{\cdot}Cr_2O_3$ (M = Co, Zn, etc.) comprise an important class of spinel materials that exhibit a variety of interesting physical properties. As a result, such materials have widespread use in applications such as catalysis,[1−3] sensing,[4,5] and as pigments.[6] In addition, they often serve as model systems for studying low temperature magnetic phenomena.

Magnetic materials are common in technology and are constantly undergoing changes to adapt to modern device requirements. In particular, advances that receive widespread attention are those that broaden the scope of these materials by utilizing their unique combination of properties. For example, $CoCr_2O_4$ is the first multiferroic material in which the electric polarization is induced by spiral magnetic order.[7] We note that multiferroics showing coupling between different types of magnetic and ferroelectric order parameters are particularly promising for technological device applications as there is the prospect of controlling the magnetic properties by an external electric field and vice versa.[8,9]

Except for tetragonal $CuCr_2O_4$ and $NiCr_2O_4$ (Jahn−Teller effect),[10] MCr_2O_4 chromites crystallize in a cubic $Fd\bar{3}m$ spinel structure and bulk versions of these materials are, without exception, normal spinels due to the large octahedral ligand field stabilization energy of Cr^{3+}.[11] This means that the crystal structure consists of either magnetic or nonmagnetic transition metal atoms occupying all of the tetrahedral 8(a) sites and magnetic chromium atoms occupying all of the octahedral 16(d) sites. In contrast, MFe_2O_4 ferrites can adopt normal, inverse, and mixed spinel structures, and it has been shown that chromites and ferrites are capable of forming solid solutions of the type $MCr_{2-x}Fe_xO_4$ over the whole range of composition, that is, $0 \leq x \leq 2$. Accordingly, the optical, magnetic, and

Received: September 1, 2011
Revised: November 22, 2011
Published: November 23, 2011

   dx.doi.org/10.1021/cm2026043 | *Chem. Mater.* 2012, 24, 155−165

Table 1. Recipes for the Synthesis of $CoCr_2O_4$, $CoCrFeO_4$, $ZnCr_2O_4$, and $ZnCrFeO_4$ Thin Films

	$Co(NO_3)_2{\cdot}6H_2O$ (mg)	$Zn(NO_3)_2{\cdot}6H_2O$ (mg)	$Cr(NO_3)_3{\cdot}9H_2O$ (mg)	$Fe(NO_3)_3{\cdot}9H_2O$ (mg)
$CoCr_2O_4$	115.5		317.7	
$CoCrFeO_4$	113.5		156.0	157.6
$ZnCr_2O_4$		114.7	308.7	
$ZnCrFeO_4$		112.9	151.8	153.3

electronic properties can be tailored through the variation of cations on the tetrahedral and octahedral coordination sites.

Apart from the spinel composition and cation distribution, it is known that physical properties can be also tailored both by controlling the size of the nanocrystalline domains and by the morphology of the material itself. Many materials, including redox-active compounds,[12,13] ferroics,[14,15] and so forth, have seen benefits from structuring on the nanoscale in that they were able to outperform their bulk counterparts.

In recent years it has been shown that polymer templating strategies are efficient routes to produce mesostructured binary and more complex oxide materials with uniform pores and a highly crystalline framework.[16−19] The formation of these materials relies on the solution phase coassembly of either preformed nanoparticles or molecular inorganic precursors with an amphiphilic polymer,[19−25] the latter acting as the structure-directing agent. The corresponding thin films can be achieved by the same coassembly methods but using an evaporation-induced self-assembly (EISA) process. This process was introduced by Brinker in the late 1990s and is still the method of choice in the synthesis of oxide thin film materials with periodicities in the sub-40 nm size range.[26]

The present work specifically focuses on $CoCr_2O_4$ and $ZnCr_2O_4$ spinel thin films as well as on equimolar solid solutions of $CoCrFeO_4$ and $ZnCrFeO_4$, materials that as we show here can be produced with ordered cubic networks of 15 nm diameter pores and tunable nanocrystalline domain sizes by utilizing a poly(ethylene-*co*-butylene)-*block*-poly(ethylene oxide) diblock copolymer, referred to as KLE.[27] We use the mesoporous $CoCr_2O_4$ thin films as model systems both to study the spinel composition on the nanoscale and to examine the magnetic properties, relative to bulk versions of cobalt chromite.

EXPERIMENTAL SECTION

Materials. $Zn(NO_3)_2{\cdot}6H_2O$ (98%), $Co(NO_3)_2{\cdot}6H_2O$ (99.99%), $Cr(NO_3)_3{\cdot}9H_2O$ (99.99%), $Fe(NO_3)_3{\cdot}9H_2O$ (99.99%), ethanol, and 2-methoxyethanol were purchased from Sigma-Aldrich. H-$[(CH_2CH_2)_{0.67}(CH_2CHCH_2CH_3)_{0.33}]_{89}(OCH_2CH_2)_{79}OH$, referred to as KLE,[27] was used as the structure-directing agent.

Synthesis. In a water-free container, 40 mg of KLE dissolved in both 1.5 mL of ethanol and 0.5 mL of 2-methoxyethanol are combined with the corresponding hydrated metal nitrate salts. Table 1 summarizes reagent masses for each type of film prepared in this work. Once the solution is homogeneous, thin films can be produced via dip-coating on polar substrates, including quartz and polished silicon wafers. Optimal conditions include relative humidities below 10% and constant withdrawal rates of 1−10 mm/s. For best results, the films are aged at 250 °C for 12 h and then annealed in air using a 45 min ramp to 700 °C.

Methods. Bright-field transmission electron microscopy (TEM) and scanning electron microscopy (SEM) images were taken with a CM30-ST microscope from Philips and a LEO Gemini 982, respectively. Atomic force microscopy (AFM) images were collected on a multimode atomic force microscope from Veeco Instruments, employing Olympus microcantilevers (resonance frequency, 300 kHz; force constant, 42 N/m). Wide-angle X-ray diffraction (WAXD) measurements were carried out on an X'Pert PRO diffractometer from PANalytical instruments. Grazing incidence small-angle X-ray scattering (GISAXS) data were collected at the German synchrotron radiation facility HASYLAB at DESY on beamline BW4 using a MarCCD area detector and a sample−detector distance of 1820 mm. X-ray photoelectron spectroscopy (XPS) spectra were acquired on a Physical Electronics ESCA 5600 spectrometer with monochromatic Al−Kα X-ray source and a multichannel detector OmniIV. The electron takeoff angle to the sample surface was adjusted to 45°. The C1s signal from adventitious hydrocarbon at 284.8 eV was used as the energy reference to correct for charging. The samples were also analyzed by time-of-flight secondary ion mass spectrometry (TOF-SIMS) using a TOF-SIMS 5 from ION-TOF GmbH. A primary ion beam of 25 keV Bi^+ was used to generate secondary ions. Sputter etching was carried out using a beam of 1 keV O^+ (I_0 = 131.1 nA). Raman spectra were acquired using the SENTERRA dispersive Raman microscope from Bruker Optics equipped with an objective from Olympus (MPlan N 50x, *FN* = 22, *NA* = 0.40) and a Nd:YAG laser (λ = 532 nm, *P* = 5 mW). Krypton physisorption measurements were conducted at 87 K on (110 ± 5) nm thick $CoCr_2O_4$ films with a total area of 47 cm^2 using the Autosorb-1-MP automated gas adsorption station from Quantachrome Corporation. Optical absorption measurements were carried out on a Perkin-Elmer Lambda 900 UV−vis−NIR spectrophotometer. A substrate made from fused silica and an aluminum mirror served as the reference for transmission and reflection measurements, respectively. Thermogravimetric analysis (TGA) data were obtained with a Netzsch STA 409 PC at a heating rate of 5 °C/min. The thermobalance was coupled to a Balzers QMG 421 quadrupole mass spectrometer. The ionization energy was 70 eV. The film thickness was determined with an Alpha Step IQ Surface Profiler from KLA Tencor. For crystal structure visualization, the software Crystal Impact Diamond version 3.2g was used. Magnetization measurements were carried out on a Quantum Design superconducting quantum interference device (SQUID) magnetometer. Magnetization as a function of temperature was measured in the range of 5−380 K with an applied field of 100 Oe. Magnetization as a function of field was measured up to a maximum field of 50 kOe.

RESULTS AND DISCUSSION

While several methods have been utilized to make MCr_2O_4 (M = Co, Zn) materials in forms other than bulk, including nanoparticles[28,29] and nanotubes,[30] to our knowledge the use of EISA to produce well-defined mesoporous versions of these oxide spinels has not yet been reported. Breakthroughs in the soft-templating synthesis of ordered porous materials with periodicities in the sub-40 nm size range over the past 10 years make EISA the method of choice in the preparation of inorganic thin films with both a mesoporous morphology and a nanocrystalline framework. The transition metal chromites and solid solutions employed in this work were produced using an EISA process. Briefly, an isotropic solution containing ethanol, 2-methoxyethanol, KLE diblock copolymer and the corresponding hydrated metal nitrate salts is dip- or spin-coated onto a polar substrate. Upon evaporation of the volatile constituents, the system coassembles to form a mesostructured inorganic/organic composite. Thermal treatment can then be used to further cross-link the inorganic wall structure, combust the KLE template, and to induce the conversion of the amorphous material to crystalline spinel. We note that the use

dx.doi.org/10.1021/cm2026043 | *Chem. Mater.* 2012, 24, 155−165

of 2-methoxyethanol as a cosolvent is not vital for the successful synthesis of these nanomaterials. The comparatively low vapor pressure of 2-methoxyethanol only helps slow down the drying process of the KLE-templated thin films, which ultimately leads to samples with more ordered structures.

As mentioned above, in this work we incorporated a poly(ethylene-*co*-butylene)-*block*-poly(ethylene oxide) diblock copolymer, also referred to as KLE (made by polymerization of ethylene oxide using "Kraton Liquid" as the macroinitiator), as the structure-directing agent.[27] Unlike the well-known Pluronic-type triblock copolymers, such as P123 and F127, KLE with its superior templating properties has been shown to be particularly suitable for the preparation of ordered mesoporous thin films with both highly crystalline walls and uniform pores.[13,18,31,32] The same synthesis method employed here failed when using Pluronic-type templates. This, however, does not imply that no mesoporous materials can be obtained but rather that the morphology is not retained when the crystalline phase is achieved. The reason for this failure is that Pluronic-type triblock copolymers produce inorganic/organic composites with only 10−20 nm repeat distances. These distances accommodate walls that are not sufficiently thick[33,34] to allow for uniform nucleation and growth of the crystalline phase while retaining nanoscale periodicity. In other words, the stable critical nucleation size of the seed crystallites often exceeds the thickness of the pore walls, and this mismatch leads to the loss of periodicity. Overall, this means that if larger nuclei are present at the onset of crystallization more restructuring of the pore-solid architecture is likely to occur. The KLE diblock copolymer, by contrast, produces wall thicknesses closer to 15 nm, which usually enables the formation of stable crystallites without the need to severely distort the pore network during crystallization.[13,31,32]

To probe the mesoporous architectures, scanning electron microscopy (SEM), transmission electron microscopy (TEM), and atomic force microscopy (AFM) were used. The combination of these techniques allows imaging of both the top surface of the films and the porous interiors. Figure 1 shows top view SEM and tapping mode AFM images of KLE-templated $CoCr_2O_4$ and $ZnCr_2O_4$ spinel thin films heated to different annealing temperatures of 600 and 700 °C. The SEM images reveal high quality cubic networks of pores averaging 15 nm in diameter, and further show that both thin film materials are crack-free at the micrometer length scale (see also low-magnification SEM images in Supporting Information, Figure S1). From these data, it is also evident that the presence of major structural defects can be ruled out and that the pores at the sample/air interface are open after removal of the polymer template and crystallization of the initially amorphous frameworks. Moreover, SEM indicates that the self-assembled $CoCr_2O_4$ samples undergo less severe restructuring during high temperature treatment than $ZnCr_2O_4$. For $ZnCr_2O_4$, this restructuring is associated with partial loss of in-plane periodicity, as can be seen in Figure 1e. Lastly, AFM shows that the hexagonal top surfaces are quite flat with a root-mean-square roughness of less than 2 nm, even after annealing at 700 °C.

We note that all materials studied in this work were prepared using approximately 30 wt % of KLE diblock copolymer with respect to the oxide spinel that is formed. The reason for this is that this value gives the best results in terms of pore ordering, wall thickness, and size of the mesopore cavities. Supporting Information, Figure S2 shows a series of top view SEM images,

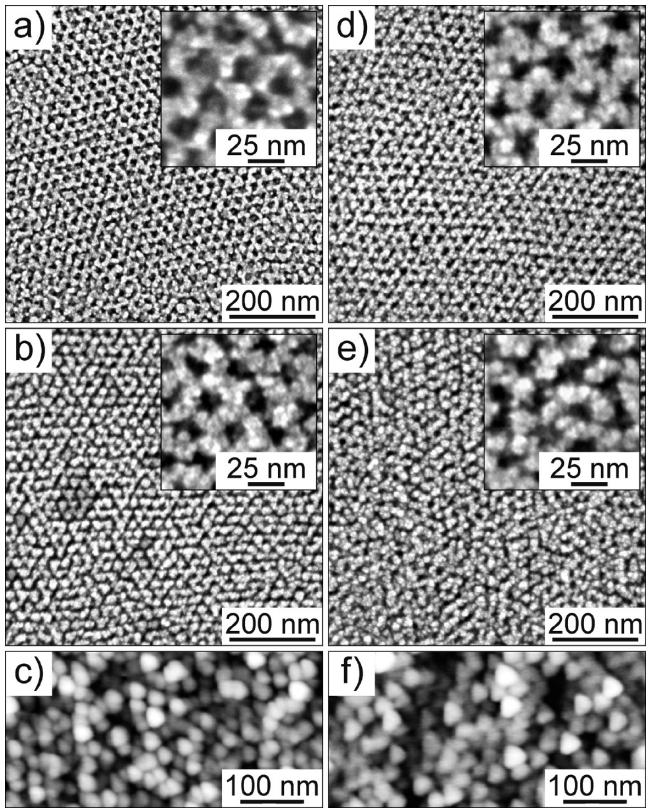

Figure 1. Morphology of KLE-templated $CoCr_2O_4$ (a−c) and $ZnCr_2O_4$ (d−f) thin films heated to 600 °C (a,d) and 700 °C (b,c,e,f). (a,b,d,e) Low-magnification top view SEM images showing open pores averaging 15 nm in diameter. Higher magnification SEM images are shown in the insets. (c,f) 3D-AFM height images. The contrast covers height variations in the 1−6 nm range.

which illustrate the influence of the KLE mass fraction on the nanoscale structure of $CoCr_2O_4$ thin films.

Figure 2 shows cross-sectional SEM and bright-field TEM images along with electron diffraction (ED) data of KLE-templated $CoCr_2O_4$ and $ZnCr_2O_4$ spinel thin films heated to 600 °C. From SEM and TEM we are able to establish that the cubic pore structures observed at the top surface of both materials persist throughout the bulk of the films. The insets in Figures 2b and d are ED patterns obtained on the same samples shown in Figures 1a and d. These patterns reveal Debye−Scherrer rings characteristic of materials with randomly oriented nanocrystalline domains. Calculated lattice spacings are in accordance with JCPDS (Joint Committee on Powder Diffraction Standards) reference cards for cochromite (no. 22-1084) and zincochromite (no. 22-1107), which provides ample evidence that both transition metal chromites adopt the spinel structure. Overall, the microscopy data in Figures 1 and 2 verify that the mesoporous morphology of the KLE-templated MCr_2O_4 thin films is retained when the spinel phase is achieved.

Figure 3 shows top view SEM and bright-field TEM images as well as ED patterns of KLE-templated $CoCrFeO_4$ and $ZnCrFeO_4$ solid solution thin films heated to the same annealing temperatures, that is, 600 and 700 °C. These data indicate that the synthesis method employed in this work can be readily extended to more complex oxides with spinel structure by substituting chromium with other isovalent metal cations of similar radius. Both the SEM and the TEM images

dx.doi.org/10.1021/cm2026043 | *Chem. Mater.* 2012, 24, 155−165

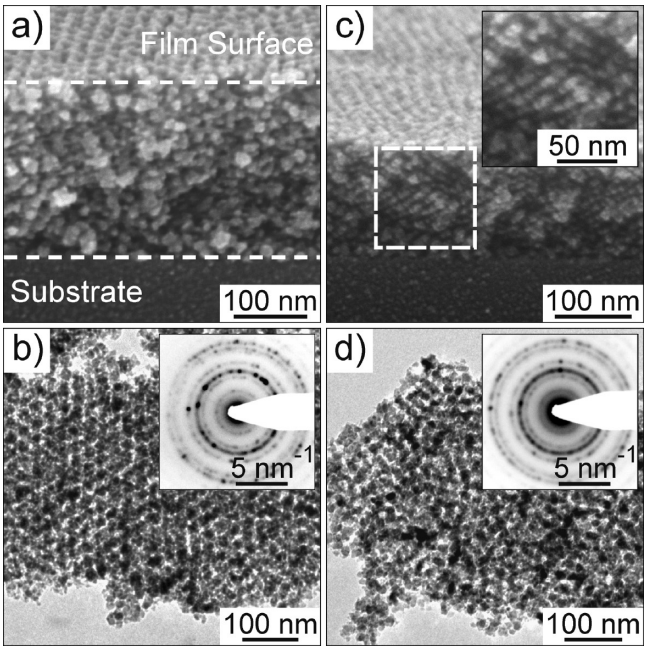

Figure 2. Morphology of KLE-templated $CoCr_2O_4$ (a,b) and $ZnCr_2O_4$ (c,d) thin films heated to 600 °C. (a,c) Cross-sectional SEM images showing that the cubic pore structures persist throughout the films. The inset in panel (c) shows a high-magnification SEM image of the region indicated by the dashed square. (b,d) Bright-field TEM images. Selected area ED patterns of the same samples in panels (b) and (d) are shown in the insets.

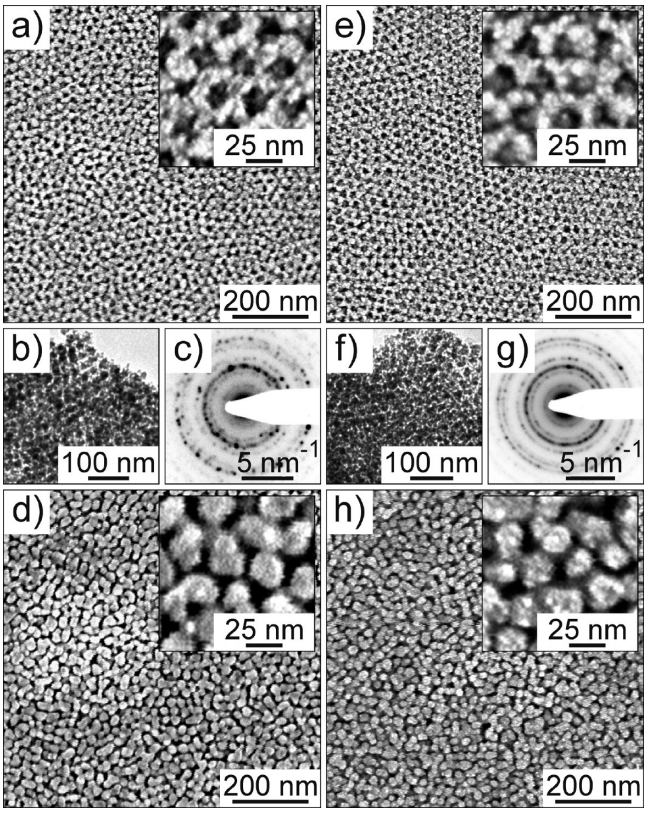

Figure 3. Morphology of KLE-templated $CoCrFeO_4$ (a–d) and $ZnCrFeO_4$ (e–h) thin films heated to 600 °C (a–c, e–g) and 700 °C (d,h). (a,d,e,h) Low-magnification SEM images showing open pores at the hexagonal top surfaces. Higher magnification top view SEM images are shown in the insets. (b,f) Bright-field TEM images. (c,g) Selected area ED patterns showing Debye–Scherrer rings characteristic of nanocrystalline materials with spinel structure.

reveal ordered cubic networks of open 15 nm diameter pores. These networks seem to be of similar quality to those of the KLE-templated MCr_2O_4 materials shown in Figures 1 and 2. From the data in Figure 3, it is also evident that the solid solution thin films are well-defined at the micrometer level (see also low-magnification SEM images in Supporting Information, Figure S1) and exhibit pore walls that consist of randomly oriented spinel crystallites. Moreover, Figures 3d and h show that the morphology is different after 700 °C because of nanocrystalline domain growth in the pore walls. This growth is accompanied by the loss of nanoscale periodicity but produces films with a unique morphology. The reason for the lack of periodicity after high temperature treatment can be attributed to a different crystallization and sintering behavior, which is more similar to that observed recently for KLE-templated MFe_2O_4 (M = Co, Zn) thin films.[35,36] Both of these ferrite spinels show extensive domain growth at temperatures above 650 °C. As a result, the crystallites are larger than the pore walls, and this mismatch leads to the restructuring shown in Figures 3d and h.

In summary, Figures 1–3 collectively establish that high quality thin films with both a mesoporous morphology and nanocrystalline framework can be produced by facile soft-templating synthesis using the diblock copolymer KLE as the structure-directing agent.

More quantitative information on the structure of all four of these large-pore mesoporous materials was obtained by grazing incidence small-angle X-ray scattering (GISAXS) and conventional SAXS experiments in Bragg–Brentano geometry. Figure 4 shows scattering patterns at an angle of incidence $\beta = 0.2°$ collected on thin films with both amorphous (250 °C) and highly crystalline (650 °C) frameworks. Samples with fully amorphous wall structures produce patterns with distinct scattering maxima that can be indexed to ordered face-centered-cubic (f-c-c) close-packed pore structures with (111) orientation. This orientation is typical of thin film materials templated using the diblock copolymer KLE and is also consistent with the electron microscopy data in Figures 1–3, in particular with the hexagonal symmetry of the various top surfaces. The same GISAXS patterns further show that the solid solution thin films exhibit a lower preferred orientation relative to the plane of the substrate than the MCr_2O_4 chromites. This result can also be explained by the partial replacement of chromium by iron and the fact that KLE-templated ferric nitrate-derived materials typically show a lower pore ordering; both $CoFe_2O_4$ and $ZnFe_2O_4$ spinel thin films reveal only distorted cubic pore networks.[35,36]

In agreement, SAXS experiments conducted in Bragg–Brentano geometry on samples heated to 250 °C show distinct reflections (see Figure 5a). These scans, however, provide only information about the periodicity in the off-plane direction. The fact that even strong second order reflections can be observed for $CoCr_2O_4$ and $ZnCr_2O_4$ thin films verifies good out-of-plane order. In contrast, SAXS patterns of $CoCrFeO_4$ and $ZnCrFeO_4$ solid solution thin films (see Supporting Information, Figure S3) reveal broadened and less defined peaks, thereby also indicating a lower degree of nanoscale periodicity than both transition metal chromites.

The elliptical shape of the GISAXS patterns in Figure 4 further indicates a large lattice contraction of the cubic pore-

dx.doi.org/10.1021/cm2026043 | Chem. Mater. 2012, 24, 155–165

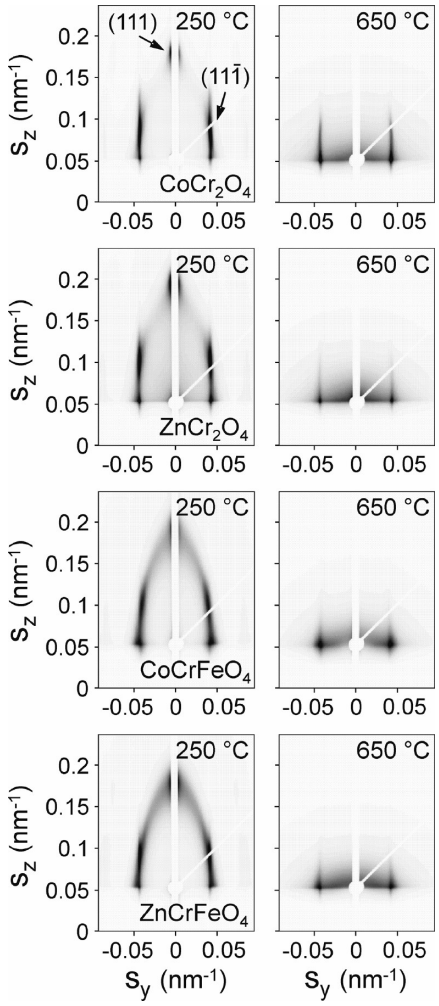

Figure 4. Synchrotron-based GISAXS on KLE-templated $CoCr_2O_4$, $ZnCr_2O_4$, $CoCrFeO_4$, and $ZnCrFeO_4$ thin films with amorphous and nanocrystalline wall structures. GISAXS patterns were collected at an angle of incidence $\beta = 0.2°$ and show the evolution of the various f-c-c pore networks upon thermal treatment. Scattering vector, ***s***, components are given in nm^{-1}.

solid architectures normal to the plane of the substrate. As expected, the in-plane contraction is negligible because the materials are pinned to the substrate. On the basis of the relative position of the (111) scattering maxima a decrease in inorganic volume of more than 70% is determined for films calcined at 250 °C for 12 h. Higher annealing temperatures do not lead to further contraction as the nitrate ligands of the different precursors used in this work are fully decomposed by 250 °C. This result is confirmed by thermogravimetric analysis-mass spectrometry (TGA-MS) data and also is consistent with previous studies on the thermal decomposition of various hydrated metal nitrates.[37] TGA-MS in the Supporting Information, Figure S4 shows that the conversion of chromium and cobalt hydroxy- and oxynitrate species, which are formed during thermal annealing, to glassy $CoCr_2O_4$ is completed after 300 °C at a heating rate of 5 °C/min.[38,39] Upon heating the samples to 650 °C to fully crystallize the pore walls, a loss of out-of-plane scattering is observed. This loss is likely due both to the small number of repeat units normal to the substrate and to the process of crystallizing the inorganic framework itself, which may slightly disrupt the nanoscale periodicity.

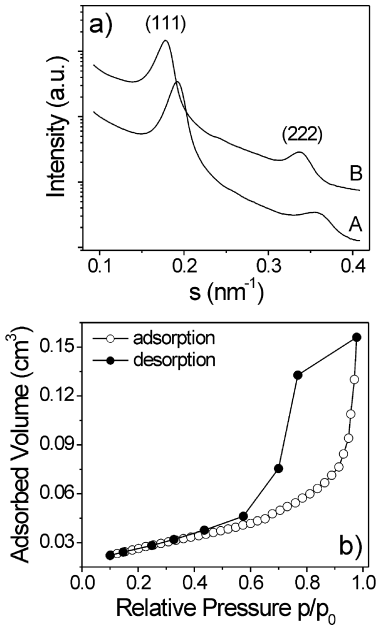

Figure 5. (a) SAXS patterns obtained on KLE-templated $ZnCr_2O_4$ (A) and $CoCr_2O_4$ (B) thin films calcined at 250 °C for 12 h. (b) Krypton adsorption−desorption isotherms of mesoporous $CoCr_2O_4$ thin films heated to 600 °C. The type-IV shape is characteristic of a material with open mesopore cavities that are interconnected through smaller necks.

Overall, the data in Figures 4 and 5a support the structure and morphology results and verify that the ordered cubic pore networks are retained after thermal treatment at 650 °C. This, in turn, provides ample evidence that the nanoscale architectures studied here can readily accommodate the spinel crystallites that form at the onset of crystallization. In this regard, we note again that the synthesis of materials that combine key features, such as well-defined porosity, high crystallinity, and thermal stability, still constitutes a major challenge to current soft- and hard-templating routes.[18,40,41] These features, however, are often a prerequisite to meet the stringent requirements imposed by many applications. The spinel materials prepared in this work show all of the aforementioned key features and thus we believe that they represent ideal model systems.

Both Brunauer−Emmett−Teller (BET) surface area and pore volume were determined by krypton physisorption measurements at 87 K (see Figure 5b). Using a saturation pressure of 13 Torr (17.3 hPa) and a cross-sectional area of 20.5 Å^2 for krypton, a BET surface area of 230 m^2/cm^3 and a pore volume of 2.4×10^{-4} cm^3 (equivalent to 45% porosity) are obtained for KLE-templated $CoCr_2O_4$ thin films heated to 600 °C. We estimate the error margin as being ±5%. Higher annealing temperatures lead to a steady reduction in pore volume because of domain growth in the pore walls. The same KLE-templated samples reveal a porosity of approximately 35% after 700 °C. This result is in agreement with both the electron microscopy and the GISAXS data showing that high temperature treatment slightly disrupts the nanoscale porosity.

To more fully characterize these materials, a series of UV−vis spectroscopy, wide-angle X-ray diffraction (WAXD), X-ray photoelectron spectroscopy (XPS), time-of-flight secondary ion mass spectrometry (TOF-SIMS), and Raman spectroscopy measurements were carried out.

dx.doi.org/10.1021/cm2026043 | *Chem. Mater.* 2012, 24, 155−165

It is known that MCr_2O_4 chromites have interesting optical properties, which might be exploited both in solid-state devices that utilize heterojunction effects[42] and in magneto-optical devices.[43,44] Moreover, it has been shown that some of these spinel oxides (e.g., $ZnCr_2O_4$) also have potential as photocatalysts for the degradation of organic pollutants.[28] For all of these applications, knowledge of the optical characteristics, including band gap energy, is crucial. The following equation can be used to describe the dependence of absorption coefficient, α, on the difference between the photon energy of incident light, $h\nu$, and the band gap energy, E_g (with $h\nu > E_g$):[45]

$$a \propto (h\nu - E_g)^n \quad (1)$$

In eq 1, n represents the type of optical transition. For $n = 1/2$, this transition is direct while $n = 2$ indicates an indirect one. Figure 6 and Supporting Information, Figure S5 show

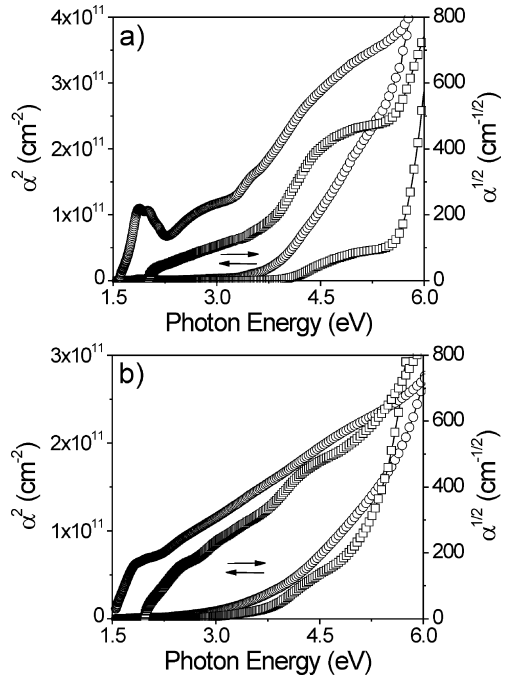

Figure 6. Plots for both direct and indirect optical transitions in KLE-templated $CoCr_2O_4$ (○) and $ZnCr_2O_4$ (□) in panel (a) and $CoCrFeO_4$ (○) and $ZnCrFeO_4$ (□) in panel (b). The various thin film materials were heated to 650 °C prior to optical characterization.

plots for both transitions and corresponding absorbance spectra, respectively.

Electronic transitions typically account for the color of transition metal compounds. Such transitions in coordination complexes can be explained by the crystal or ligand field theory. Depending on the oxidation state of the metal ion(s), the coordination geometry and the nature of the ligands surrounding the metal ion(s), d-d transitions (spin allowed) as well as oxygen−metal and heteronuclear (metal−metal) charge transfer transitions can occur.[46] Stoichiometric $ZnCr_2O_4$ has been shown to possess seven absorption bands in the visible spectrum at ∼419 nm (2.96 eV), 440 nm (2.82 eV), 489 nm (2.54 eV), 573 nm (2.16 eV), 660 nm (1.88 eV), 697 nm (1.78 eV), and 725 nm (1.71 eV) resulting from various d-d transitions in octahedrally coordinated Cr^{3+}.[47] These transitions lead to a greenish gray color. We, however, find more of a brownish color for our KLE-templated $ZnCr_2O_4$ materials, which might be due to some type of metal atom non-stoichiometry (e.g., $Zn_{1+x}Cr_{2-x}O_4$ due to hole doping associated with the oxidation of a small fraction of Cr^{3+} to Cr^{4+}).[48] This hypothesis is chemically reasonable since the materials employed in this work are solution processed via sol−gel methods and thus they should contain some defects (see also section on XPS below). In addition, it has been shown that there are two broad bands in the ultraviolet (UV) centered at about 3.50 eV (354 nm) and 5.80 eV (214 nm). These bands are assumed to arise because of oxygen−metal charge transfer since metal−metal transitions are not possible in $ZnCr_2O_4$. From Figure 6a it can be seen that both transitions occur at energies similar to those reported in the literature.[28,49] We note that such charge transfer absorptions can be up to 2 orders of magnitude stronger than d-d transitions, which is the case for the KLE-templated materials studied here.

Recently, Peng et al.[28] and Parhi et al.[49] estimated the optical band gap energy from data for a direct transition as being approximately 3.40 eV (365 nm). The presence of a direct band gap is in agreement with predictions although density functional theory calculations suggest a lower value of 2.90 eV (428 nm).[50] We assume that the deviation from the theoretically determined value is due to superposition from other transitions; according to Singh and co-workers the band gap is located between two d-d transitions.[50] Overall, it is evident that both the wide variety of d-d and charge transfer transitions in MCr_2O_4 chromites and the fact that some of these transitions can be obscured by overlapping bands make definitive assignments, including band gap determination, very difficult. From the data in Figure 6a and Supporting Information, Figure S5 we obtain a direct band gap at (3.20 ± 0.05) eV (equivalent to ∼387 nm light), which is in fair agreement with the reported calculated value. The slight blue-shift is not surprising as the KLE-templated materials are nanocrystalline, and thus a shift may be expected.

In contrast to $ZnCr_2O_4$, the mesoporous $CoCr_2O_4$ thin films show a mint green color while bulk versions of this material are bluish green. We attribute this change in color to a slight broadening and shift of the absorption maxima although a metal atom nonstoichiometry could certainly affect the optical properties as well. The positions of these maxima in the visible region of the spectrum are as follows: ∼450 nm (2.76 eV), 620 nm (2.0 eV), and 660 nm (1.88 eV).[51] In addition, we observe two UV-centered bands at about 3.70 eV (335 nm) and 5.80 eV (214 nm), which likely arise because of charge transfer absorptions. Lastly, it is also apparent from Figure 6a that the lack of the characteristic shape of the plot, $\alpha^{1/2}$ versus photon energy, argues against an indirect optical transition in nanocrystalline $CoCr_2O_4$. Thus, we estimate the band gap energy from data for the direct transition as being (3.10 ± 0.05) eV (equivalent to ∼400 nm light).

Apart from the KLE-templated transition metal chromites, we also examined the mesoporous $ZnCrFeO_4$ and $CoCrFeO_4$ solid solution thin films. These materials reveal reddish brown and golden brown colors, respectively. However, Figure 6b and Supporting Information, Figure S5 clearly show that the optical band gap energies cannot be determined on the basis of these data alone. Perhaps one of the reasons for this is the presence of numerous overlapping bands. In this regard, we note again that the optical characteristics of such solid solution compounds in the visible spectrum are determined by both d-d transitions in tetrahedrally coordinated Co^{2+} and Fe^{3+} and

dx.doi.org/10.1021/cm2026043 | Chem. Mater. 2012, 24, 155−165

octahedrally coordinated Co^{2+}, Cr^{3+}, and Fe^{3+}, which emphasizes the underlying complexity of the data.

As mentioned above, the transition metal chromites and solid solutions prepared in this work crystallize in a cubic spinel structure that possesses 56 atoms per unit cell, equivalent to 8 formula units. Both $CoCr_2O_4$ and $ZnCr_2O_4$ are normal spinels. The crystal structure of these materials consists of either magnetic Co^{2+} ($3d^7$) or nonmagnetic Zn^{2+} ($3d^{10}$) ions occupying all of the tetrahedral (A) coordination sites and magnetic Cr^{3+} ($3d^3$) ions occupying all of the octahedral (B) sites (see Figure 7).

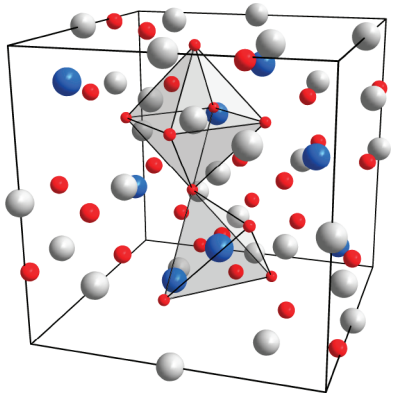

Figure 7. Scheme of the $CoCr_2O_4$ unit cell. Chromium atoms occupying the octahedral 16(d) sites are shown in light gray, cobalt atoms on tetrahedral 8(a) sites in blue, and oxygen atoms on 32(e) sites in red. The different coordination spheres are indicated by polyhedra.

The cation distribution is typically analyzed in terms of the inversion parameter, λ, with $\{[A_{1-\lambda}B_\lambda]_{tet}[A_\lambda B_{2-\lambda}]_{oct}O_4\}$. The two ordered configurations with $\lambda = 0$ (normal spinel) and $\lambda = 1$ (inverse spinel) are commonly observed for $CoCr_2O_4$ and $CoFe_2O_4$, respectively, whereas many other materials that adopt the spinel structure exhibit random distributions. The cation distribution is determined by several factors, such as ionic radii, electrostatic repulsion, nature of the covalent bonding, ligand field stabilization energy, and so forth.[52] In general, however, it is reasonable to expect a lower degree of cation ordering for spinel materials prepared by chemical solution deposition rather than physical deposition techniques.

It is known that all MCr_2O_4 chromites in bulk form are, without exception, normal spinels due to the large octahedral ligand field stabilization energy of Cr^{3+} (high-spin state). In contrast, MFe_2O_4 ferrites can adopt normal, inverse, and mixed spinel structures. The reason for this is that Fe^{3+} ($3d^5$) exhibits no ligand field stabilization and thus there is no preference for either coordination site. Moreover, it has also been shown that Cr^{3+} can be substituted by other isovalent metal cations of similar radius, such as magnetic Fe^{3+} and nonmagnetic Ga^{3+}.[53] Chromium and iron are particularly suitable since they are capable of forming solid solutions of the type $MCr_{2-x}Fe_xO_4$ (M = Co, Zn) over the whole range of composition.[54] In this regard, it is important to note that Zn^{2+}/Fe^{3+} mixing on tetrahedral coordination sites in not expected because both $ZnCr_2O_4$ and $ZnFe_2O_4$ are normal spinels. However, this type of disorder is very likely for $CoCr_{2-x}Fe_xO_4$ since $CoFe_2O_4$ is a material with inverse spinel structure.

Figures 8a and b show WAXD patterns of KLE-templated $CoCr_2O_4$ and $CoCrFeO_4$ thin films heated to different

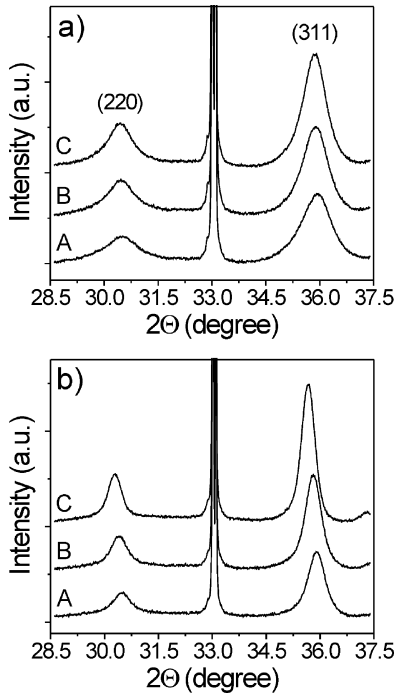

Figure 8. (a) WAXD patterns obtained on KLE-templated $CoCr_2O_4$ thin films heated to 600 °C (A), 650 °C (B), and 700 °C (C). (b) WAXD patterns of KLE-templated $CoCrFeO_4$ thin films heated to 500 °C (A), 600 °C (B), and 700 °C (C).

annealing temperatures. The crystallization begins at approximately 550 °C for $CoCr_2O_4$ and 500 °C for $CoCrFeO_4$. The lower crystallization temperature of $CoCrFeO_4$ can be ascribed to the fact that, despite equimolar composition, these solid solution thin films show a behavior somewhat similar to that found for KLE-templated $CoFe_2O_4$.[35] Applying the Scherrer equation to the full width at half-maximum intensity of the most intense (311) peak indicates that the nanocrystalline spinel domains slowly grow as the temperature is increased. The domain sizes start at 6 nm for $CoCr_2O_4$ and 14 nm for $CoCrFeO_4$ and reach 13 and 19 nm, respectively, at 700 °C. WAXD patterns obtained on a KLE-templated $CoCr_2O_4$ powder sample heated to temperatures of less than 550 °C is shown in Supporting Information, Figure S6a. These data reveal only an amorphous halo because the sol–gel derived $CoCr_2O_4$ materials are fully amorphous below 550 °C. However, the amorphous halo is found to shift toward lower d-spacings (higher angles) as the temperature is increased from 100 to 300 °C. This result is consistent with the TGA-MS data and indicates the conversion of weakly cross-linked chromium and cobalt hydroxy- and oxynitrate species to glassy $CoCr_2O_4$. As opposed to $CoCr_2O_4$, KLE-templated $ZnCr_2O_4$ and $ZnCrFeO_4$ thin films both begin to crystallize at approximately 500 °C (see Supporting Information, Figure S6). For these materials we find domain sizes that are tunable from 6 to 9 nm ($ZnCr_2O_4$) and 11 to 16 nm ($ZnCrFeO_4$). From the data in Figure 8 and Supporting Information, Figure S6b,c, it is evident that the solid solutions exhibit larger crystallites than the bare transition metal chromites, which helps explain the finding that the nanoscale periodicity of these spinel thin films is not retained after thermal treatment at 700 °C. For $CoCr_2O_4$ and $ZnCr_2O_4$, extensive domain growth due to sintering is observed at annealing temperatures above 700 °C. Lastly, it can be seen from Figure 8b that the diffraction peaks of $CoCrFeO_4$ shift

dx.doi.org/10.1021/cm2026043 | Chem. Mater. 2012, 24, 155–165

toward larger *d*-spacings as the annealing temperature is increased from 500 to 700 °C. Since such a shift is not observed for $ZnCrFeO_4$, we assume that it is related to Co^{2+}/Fe^{3+} mixing on the tetrahedral coordination sites, that is, cation redistribution at elevated temperatures.

In the ensuing sections we specifically focus on KLE-templated $CoCr_2O_4$ thin films. The high quality of the nanocrystalline $CoCr_2O_4$ frameworks is further evidenced by XPS, Raman spectroscopy, and TOF-SIMS. Figure 9a shows a typical XPS survey spectrum. Apart from a weak carbon C1s peak, which we associate with adventitious hydrocarbon, only chromium, cobalt, and oxygen core levels are observed. Figures 9b and c show high-resolution scans of the Co2p and Cr2p regions. These spectra contain main peaks at binding energies of (796.1 ± 0.05) eV and (780.4 ± 0.05) eV for the $Co2p_{1/2}$ and $Co2p_{3/2}$ lines, respectively, and (585.7 ± 0.05) eV and (576.2 ± 0.05) eV for the $Cr2p_{1/2}$ and $Cr2p_{3/2}$ lines, respectively. Both the peak positions and separations ($\Delta Cr2p$ = 9.5 eV; $\Delta Co2p$ = 15.7 eV) are in agreement with reported measured values for $CoCr_2O_4$ and indicate single oxidation states which are identified as Co^{2+} and Cr^{3+}.[55,56] The presence of Co^{2+} is further supported by the appearance of strong satellite peaks about 6 eV higher in binding energy than the main peaks. We also find a satellite peak in the Cr2p spectrum, which overlaps with the $p_{1/2}$ line. This peak is about 11 eV higher in binding energy than the $p_{3/2}$ line and is characteristic of Cr^{3+}. Elemental analyses carried out by comparing the area of the various Co and Cr levels reveal atomic chromium-to-cobalt ratios close to the expected value of 2.0 for stoichiometric $CoCr_2O_4$. XPS spectra obtained on KLE-templated $ZnCr_2O_4$ thin films heated to 650 °C are shown in Supporting Information, Figure S7.

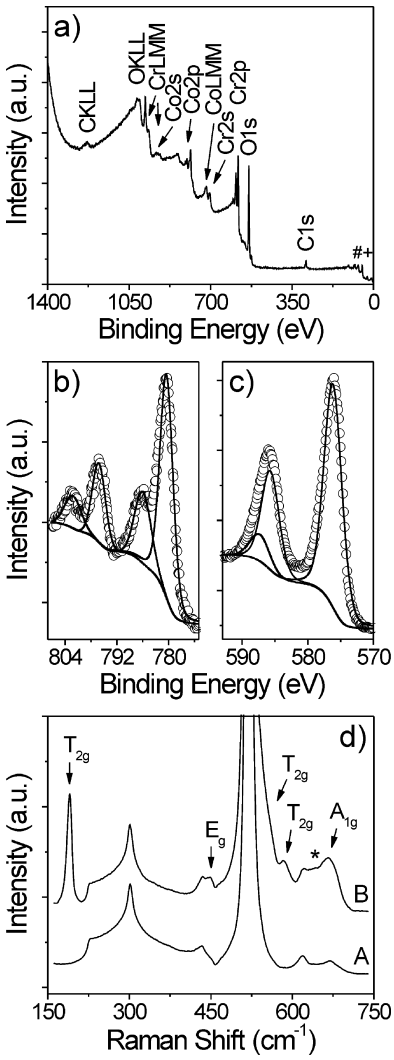

Figure 9. (a) Typical XPS survey spectrum of KLE-templated $CoCr_2O_4$ thin films heated to 650 °C. The Co3s/Cr3s/Co3p/Cr3p and O2s regions are indicated by (#) and (+), respectively. (b,c) High-resolution XPS scans of the Co2p and Cr2p core levels. Solid lines are Gaussian–Lorentzian fits to the data assuming Shirley background. (d) Raman spectra obtained on both a bare (100)-oriented silicon wafer (A) and a nanocrystalline $CoCr_2O_4$ thin film on silicon wafer (B). The asterisk at ~640 cm^{-1} indicates an otherwise forbidden Raman mode.

Since both X-ray diffraction and X-ray photoelectron spectroscopy can be insensitive to poorly crystalline materials as well as trace amounts of second phases and lattice distortions, Raman measurements were also carried out. We are unaware of any Raman studies on nanocrystalline $CoCr_2O_4$ materials in the literature. Typical Raman spectra of KLE-templated $CoCr_2O_4$ spinel thin films on both (100)-oriented silicon and quartz substrates are shown in Figure 9d and Supporting Information, Figure S8, respectively. According to group theory, $CoCr_2O_4$ with purely normal spinel structure has five Raman-active phonon modes ($\Gamma = 1A_{1g} + 1E_g + 3F_{2g}$ or alternatively $3T_{2g}$).[57] All of these modes can be observed at approximately 189 cm^{-1} (T_{2g}), 448 cm^{-1} (E_g), 536 cm^{-1} (T_{2g}), 583 cm^{-1} (T_{2g}), and 666 cm^{-1} (A_{1g}). The band assignment is in agreement with data reported previously for both polycrystalline[58,59] and single-crystalline[60,61] $CoCr_2O_4$ and $ZnCr_2O_4$ materials. In addition to these bands, however, we find one more at approximately 640 cm^{-1}, which is not predicted by group theory. The appearance of this band is presumably related either to some kind of cation distribution among the tetrahedral and octahedral sites (so-called antisite defect), as reported by Wang et al.,[58] or to the presence of a small fraction of Cr^{4+} on the octahedral sites, as reported by Stanojevic et al.[59] Overall, the results with WAXD, XPS, and Raman spectroscopy lead us to propose that all characteristics of the self-assembled $CoCr_2O_4$ samples studied in this work can be associated with the desired spinel phase; larger fluctuations in composition and the presence of second phases, such as Cr_2O_3 or α-CrO(OH), which could potentially be formed during thermal treatment, can both be ruled out.

The TOF-SIMS profiles of KLE-templated $CoCr_2O_4$ and $CoCrFeO_4$ thin films in Figures 10a and b show the distribution of Co^+, Cr^+, Fe^+, Si^+, and C^+ as a function of depth from the top surface. Both profiles collectively verify that the transition metal ions are homogeneously distributed throughout the bulk of the films and that the KLE diblock copolymer is removed after high temperature annealing. Only minor amounts of hydrocarbons can be detected at the sample/air and sample/substrate interfaces, which is in agreement with the XPS results. From Figure 10b, it is also apparent that the Fe^+ and Co^+ signal intensities slightly increase near the sample/substrate interface. This, however, neither implies that these ions are enriched at the interface nor that they diffuse into the silicon substrate during thermal treatment. The reason for the growth of both signals is the different chemical environment, which is known to have a profound effect on the ionization probability. The fact that the Si^+ signal intensity in Figure 10a

dx.doi.org/10.1021/cm2026043 | *Chem. Mater.* 2012, 24, 155–165

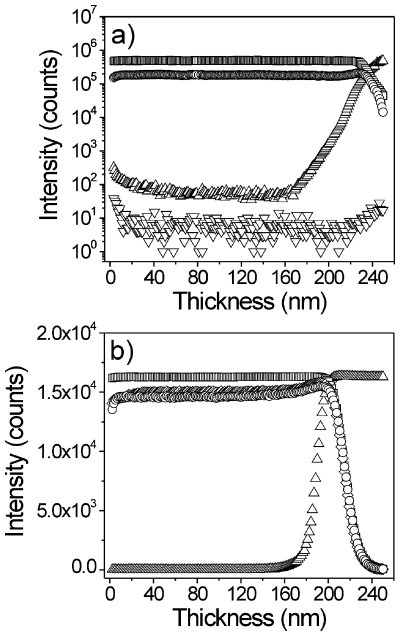

Figure 10. TOF-SIMS depth profiles of KLE-templated $CoCr_2O_4$ (a) and $CoCrFeO_4$ (b) spinel thin films on (100)-oriented silicon wafer showing the distribution of Cr^+ (□), Fe^+ (◇), Co^+ (○), Si^+ (△), and C^+ (▽). Note that the Fe^+ and Co^+ signal intensities are superimposed in panel (b).

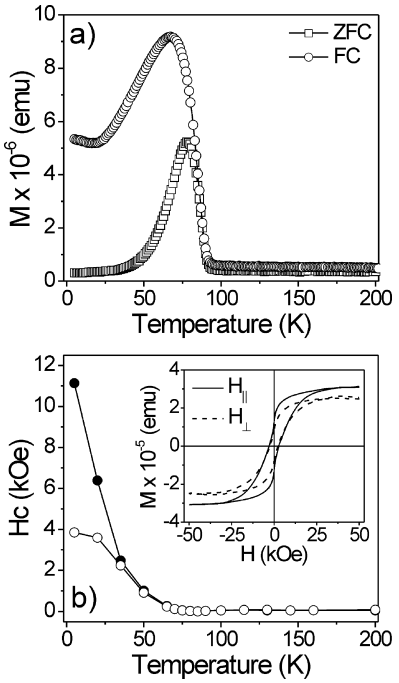

Figure 11. Magnetic properties of KLE-templated $CoCr_2O_4$ thin films heated to 650 °C. (a) Zero field cooled (ZFC) and field cooled (FC) curves (H = 100 Oe). (b) Coercivity versus temperature for samples oriented both with the plane of the substrate perpendicular (open symbols) and parallel (solid symbols) to the external magnetic field. In- and out-of-plane hysteresis experiments at 35 K are shown in the inset of panel (b).

begins to increase at a depth of 170 nm already is not fully understood at this point, but might be related to diffusion of silicon across the interior of the $CoCr_2O_4$ thin films at elevated temperatures; mobile species are always enriched at interfaces because of surface energy minimization reasons. This would also help explain the higher Si^+ signal intensity at the sample/air interface.

Magnetic properties of KLE-templated $CoCr_2O_4$ thin films heated to 650 °C were investigated using a SQUID magnetometer. The average spinel domain size is 10 nm at this annealing temperature. Temperature-dependent magnetization data were obtained from 5 to 300 K under a magnetic field of 100 Oe. Figure 11a shows typical zero field cooled (ZFC) and field cooled (FC) curves. For these measurements, the magnetization was continuously recorded as a function of increasing temperature after cooling the samples to 5 K under zero field and an applied field of 100 Oe, respectively. From the data in Figure 11a, it can be seen that both curves collapse at temperatures above 80 K. Below this temperature, irreversibilities are observed with $M_{ZFC} < M_{FC}$. The ZFC curve shows an initial low magnetization up to ~50 K, increasing thereafter until it reaches a maximum at about 77 K. This maximum can be associated with the blocking temperature, T_B, of the nanocrystalline $CoCr_2O_4$ spinel material. Bulk versions of cobalt chromite are known to develop long-range ferrimagnetic order below 94 K.[62,63] In contrast, the ferrimagnetic-paramagnetic phase transition in KLE-templated thin films appears at T_C = 85 K. This result is consistent with reported measured values for $CoCr_2O_4$ nanoparticles, and the shift in T_C has been attributed to a finite-size effect.[63] However, the observed features in $M(T)$ suggest significant competition between short- and long-range magnetic interactions in the nanocrystalline domains of the mesoporous thin film material. The kink in the FC curve at about 24 K indicates a second phase transition, in agreement with previous findings. This transition is associated with a spin reorientation of the magnetic structure (spiral order of spins).[7,64] The measured value for T_{Spiral} is slightly lower than that observed in the bulk (T_{Spiral} ~ 31 K), suggesting that the mesoporous morphology of the $CoCr_2O_4$ thin films tends to stabilize the out-of-plane magnetization component, as shown recently for KLE-templated $CoFe_2O_4$ samples.[35]

Coercive fields, H_C, obtained from hysteresis experiments at temperatures ranging between 5 and 300 K on thin films oriented both perpendicular to the external magnetic field and with the plane of the substrate parallel to the field are shown in Figure 11b. Typical angular dependent hysteresis curves at 35 K are shown in the inset of Figure 11b. We note that the (100)-oriented silicon wafers used as substrates in this work were also investigated to subtract their response; a diamagnetic susceptibility of approximately 1.5×10^{-7} emu/(Oe g) with a small decrease at low temperatures is obtained. From the data in Figure 11b, it is evident that orientation has no effect on H_C at temperatures above T_{Spiral}. This is in agreement with the existence of a distinct out-of-plane magnetization component due to both the complex ferrimagnetic spin order in $CoCr_2O_4$ materials and the mesoporous morphology of the KLE-templated thin films and the associated strain anisotropy.[35]

■ CONCLUSIONS

In summary, highly ordered mesoporous $CoCr_2O_4$ and $ZnCr_2O_4$ spinel thin films with both tunable nanocrystalline domain sizes and uniform 15 nm diameter pores have been successfully prepared through coassembly strategies using a poly(ethylene-*co*-butylene)-*block*-poly(ethylene oxide) diblock copolymer as the structure-directing agent and hydrated

dx.doi.org/10.1021/cm2026043 | *Chem. Mater.* 2012, 24, 155–165

nitrates as the inorganic precursors. This approach further provides an efficient route to produce mesoporous solid solutions of the type $MCr_{2-x}Fe_xO_4$ by substituting Cr^{3+} with isovalent Fe^{3+} ions. Electron microscopy, krypton physisorption, GISAXS, and WAXD studies collectively verify that the initially amorphous wall structures can be fully crystallized while retaining nanoscale porosity. The structure and morphology results also show that the materials employed in this work are homogeneous at both the nanoscale and the microscale. In addition, Raman, XPS, and TOF-SIMS data suggest that the KLE-templated $CoCr_2O_4$ thin films can be produced in phase-pure form and that they contain only minor defects. Magnetization studies further establish the high quality of the nanocrystalline $CoCr_2O_4$ thin films. Samples with an average spinel domain size of 10 nm show two phase transitions due to the presence of both long-range ferrimagnetic order and spiral magnetic order at low temperatures.

Overall, this research demonstrates an interesting class of mesoporous materials. It is envisioned that the open pore cavities will facilitate the formation of novel nanocomposites, which could pave the way for innovative device design. These results are exciting given the rapid advancing trend toward devices based on magnetically exchange-coupled composite materials.

■ ASSOCIATED CONTENT

Supporting Information

Low-magnification SEM images and absorbance spectra of all thin film materials. SAXS patterns of $ZnCrFeO_4$ and $CoCrFeO_4$. WAXD patterns of $ZnCr_2O_4$ and $ZnCrFeO_4$. XPS spectra of $ZnCr_2O_4$. Raman spectrum of $CoCr_2O_4$ on quartz. TGA-MS and WAXD data of $CoCr_2O_4$ in powder format. This material is available free of charge via the Internet at http://pubs.acs.org.

■ AUTHOR INFORMATION

Corresponding Author

*E-mail: torsten.brezesinski@phys.chemie.uni-giessen.de.

■ ACKNOWLEDGMENTS

The work at Giessen was in part supported by the Fonds der Chemischen Industrie. C.T.S. acknowledges the FCT for a doctoral grant SFRH/BD/38290/2007. The authors thank Anneliese Heilig, Jan Haetge, Juergen Janek, Jan Perlich, Bernd M. Smarsly, Bruno K. Meyer, and Christoph Weidmann for their assistance in materials preparation and measurements. Portions of this research were carried out at the German synchrotron radiation facility HASYLAB at DESY.

■ REFERENCES

(1) Fino, D.; Russo, N.; Saracco, G.; Specchia, V. *J. Catal.* **2006**, *242*, 38−47.
(2) Kim, D.-C.; Ihm, S.-K. *Environ. Sci. Technol.* **2001**, *35*, 222−226.
(3) Zavyalova, U.; Nigrovski, B.; Pollok, K.; Langenhorst, F.; Müller, B.; Scholz, P.; Ondruschka, B. *Appl. Catal., B* **2008**, *83*, 221−228.
(4) Bayhan, M.; Hashemi, T.; Brinkman, A. W. *J. Mater. Sci.* **1997**, *32*, 6619−6623.
(5) Yokomizo, Y.; Uno, S.; Harata, M.; Hiraki, H.; Yuki, K. *Sens. Actuators* **1983**, *4*, 599−606.
(6) Berry, F. J.; Costantini, N.; Smart, L. E. *Waste Manage.* **2002**, *22*, 761−772.
(7) Yamasaki, Y.; Miyasaka, S.; Kaneko, Y.; He, J.-P.; Arima, T.; Tokura, Y. *Phys. Rev. Lett.* **2006**, *96*, 207204.
(8) Eerenstein, W.; Mathur, N. D.; Scott, J. F. *Nature* **2006**, *442*, 759−765.
(9) Cheong, S. W.; Mostovoy, M. *Nat. Mater.* **2007**, *6*, 13−20.
(10) Crottaz, O.; Kubel, F.; Schmid, H. *J. Mater. Chem.* **1997**, *7*, 143−146.
(11) Oneill, H. S. C.; Navrotsky, A. *Am. Mineral.* **1984**, *69*, 733−753.
(12) Arico, A. S.; Bruce, P.; Scrosati, B.; Tarascon, J.-M.; Van Schalkwijk, W. *Nat. Mater.* **2005**, *4*, 366−377.
(13) Brezesinski, K.; Wang, J.; Haetge, J.; Reitz, C.; Steinmueller, S. O.; Tolbert, S. H.; Smarsly, B. M.; Dunn, B.; Brezesinski, T. *J. Am. Chem. Soc.* **2010**, *132*, 6982−6990.
(14) Zheng, H.; Wang, J.; Lofland, S. E.; Ma, Z.; Mohaddes-Ardabili, L.; Zhao, T.; Salamanca-Riba, L.; Shinde, S. R.; Ogale, S. B.; Bai, F.; Viehland, D.; Jia, Y.; Schlom, D. G.; Wuttig, M.; Roytburd, A.; Ramesh, R. *Science* **2004**, *303*, 661−663.
(15) Seidel, J.; Martin, L. W.; He, Q.; Zhan, Q.; Chu, Y. H.; Rother, A.; Hawkridge, M. E.; Maksymovych, P.; Yu, P.; Gajek, M.; Balke, N.; Kalinin, S. V.; Gemming, S.; Wang, F.; Catalan, G.; Scott, J. F.; Spaldin, N. A.; Orenstein, J.; Ramesh, R. *Nat. Mater.* **2009**, *8*, 229−234.
(16) Yang, P. D.; Zhao, D.; Margolese, D. I.; Chmelka, B. F.; Stucky, G. D. *Chem. Mater.* **1999**, *11*, 2813−2826.
(17) Choi, S. Y.; Mamak, M.; Coombs, N.; Chopra, N.; Ozin, G. A. *Adv. Funct. Mater.* **2004**, *14*, 335−344.
(18) Grosso, D.; Boissiere, C.; Smarsly, B.; Brezesinski, T.; Pinna, N.; Albouy, P. A.; Amenitsch, H.; Antonietti, M.; Sanchez, C. *Nat. Mater.* **2004**, *3*, 787−792.
(19) Sanchez, C.; Boissiere, C.; Grosso, D.; Laberty, C.; Nicole, L. *Chem. Mater.* **2008**, *20*, 682−737.
(20) Kresge, C. T.; Leonowicz, M. E.; Roth, W. J.; Vartuli, J. C.; Beck, J. S. *Nature* **1992**, *359*, 710−712.
(21) Yang, H.; Kuperman, A.; Coombs, N.; Mamiche-Afara, S.; Ozin, G. A. *Nature* **1996**, *379*, 703−705.
(22) Ciesla, U.; Schuth, F. *Microporous Mesoporous Mater.* **1999**, *27*, 131−149.
(23) Soler-illia, G. J. D.; Sanchez, C.; Lebeau, B.; Patarin, J. *Chem. Rev.* **2002**, *102*, 4093−4138.
(24) Ba, J. H.; Polleux, J.; Antonietti, M.; Niederberger, M. *Adv. Mater.* **2005**, *17*, 2509−2512.
(25) Li, D. L.; Zhou, H. S.; Honma, I. *Nat. Mater.* **2004**, *3*, 65−72.
(26) Brinker, C. J.; Lu, Y. F.; Sellinger, A.; Fan, H. Y. *Adv. Mater.* **1999**, *11*, 579−585.
(27) Thomas, A.; Schlaad, H.; Smarsly, B.; Antonietti, M. *Langmuir* **2003**, *19*, 4455−4459.
(28) Peng, C.; Gao, L. *J. Am. Ceram. Soc.* **2008**, *91*, 2388−2390.
(29) Cui, H. T.; Zayat, M.; Levy, D. *J. Sol-Gel Sci. Technol.* **2005**, *35*, 175−181.
(30) Raidongia, K.; Rao, C. N. R. *J. Phys. Chem. C* **2008**, *112*, 13366−13371.
(31) Smarsly, B.; Grosso, D.; Brezesinski, T.; Pinna, N.; Boissiere, C.; Antonietti, M.; Sanchez, C. *Chem. Mater.* **2004**, *16*, 2948−2952.
(32) Wang, Y. D.; Brezesinski, T.; Antonietti, M.; Smarsly, B. *ACS Nano* **2009**, *3*, 1373−1378.
(33) Feng, P. Y.; Bu, X. H.; Pine, D. J. *Langmuir* **2000**, *16*, 5304−5310.
(34) Flodstrom, K.; Alfredsson, V. *Microporous Mesoporous Mater.* **2003**, *59*, 167−176.
(35) Quickel, T. E.; Le, V. H.; Brezesinski, T.; Tolbert, S. H. *Nano Lett.* **2010**, *10*, 2982−2988.
(36) Haetge, J.; Suchomski, C.; Brezesinski, T. *Inorg. Chem.* **2010**, *49*, 11619−11626.
(37) Cseri, T.; Bekassy, S.; Kenessey, G.; Liptay, G.; Figueras, F. *Thermochim. Acta* **1996**, *288*, 137−154.
(38) Mansour, S. A. A. *Mater. Chem. Phys.* **1994**, *36*, 317−323.
(39) Malecki, A.; Malecka, B.; Gajerski, R.; Labus, S. *J. Therm. Anal. Calorim.* **2003**, *72*, 135−144.
(40) Schuth, F. *Chem. Mater.* **2001**, *13*, 3184−3195.
(41) Yen, H.; Seo, Y.; Guillet-Nicolas, R.; Kaliaguine, S.; Kleitz, F. *Chem. Commun.* **2011**, *47*, 10473−10475.

(42) Yan, J. H.; Zhang, L.; Yang, H. H.; Tang, Y. G.; Lu, Z. G.; Guo, S. L.; Dai, Y. L.; Han, Y.; Yao, M. H. *Sol. Energy* **2009**, *83*, 1534−1539.
(43) Ohgushi, K.; Okimoto, Y.; Ogasawara, T.; Miyasaka, S.; Takura, Y. *J. Phys. Soc. Jpn.* **2008**, *77*, 034713.
(44) Polyakova, K. P.; Polyakov, V. V.; Seredkin, V. A.; Patrin, G. S. *Tech. Phys. Lett.* **2011**, *37*, 109−111.
(45) Hagfeldt, A.; Gratzel, M. *Chem. Rev.* **1995**, *95*, 49−68.
(46) Keppler, H. *Phys. Chem. Miner.* **1996**, *23*, 288−296.
(47) Szymczak, H.; Wardzynski, W.; Pajaczkowska, A. *J. Magn. Magn. Mater.* **1980**, *15*−*8*, 841−842.
(48) Dutton, S. E.; Huang, Q.; Tchernyshyov, O.; Broholm, C. L.; Cava, R. J. *Phys. Rev. B* **2011**, *83*, 064407.
(49) Parhi, P.; Manivannan, V. *J. Eur. Ceram. Soc.* **2008**, *28*, 1665−1670.
(50) Singh, N.; Rhee, J. Y. *J. Korean Phys. Soc.* **2010**, *57*, 1233−1237.
(51) Fernandez, A. L.; de Pablo, L. *Pigm. Res. Technol.* **2002**, *31*, 350−356.
(52) Oneill, H. S. C.; Navrotsky, A. *Am. Mineral.* **1983**, *68*, 181−194.
(53) Yunus, S. M.; Azad, A. K.; Eriksson, S.-G.; Eriksen, J.; Rundlof, H.; Mathieu, R. *Phys. B* **2003**, *337*, 323−332.
(54) Hankare, P. P.; Sankpal, U. B.; Patil, R. P.; Mulla, I. S.; Lokhande, P. D.; Gajbhiye, N. S. *J. Alloys Compds.* **2009**, *485*, 798−801.
(55) Haber, J.; Nowotny, J.; Sikora, I.; Stoch, J. *Appl. Surf. Sci.* **1984**, *17*, 324−330.
(56) Kumar, L.; Mohanty, P.; Shripathi, T.; Rath, C. *Nanosci. Nanotechnol. Lett.* **2009**, *1*, 199−203.
(57) White, W. B.; Deangelis, B. A. *Spectrochim. Acta, Part A* **1967**, *A23*, 985−995.
(58) Wang, Z. W.; Lazor, P.; Saxena, S. K.; Artioli, G. *J. Solid State Chem.* **2002**, *165*, 165−170.
(59) Stanojevic, Z. V. M; Romcevic, N.; Stojanovic, B. *J. Eur. Ceram. Soc.* **2007**, No. 27, 903−907.
(60) Lutz, H. D.; Muller, B.; Steiner, H. J. *J. Solid State Chem.* **1991**, *90*, 54−60.
(61) Kant, C.; Deisenhofer, J.; Rudolf, T.; Mayr, F.; Schrettle, F.; Loidl, A.; Gnezdilov, V.; Wulferding, D.; Lemmens, P.; Tsurkan, V. *Phys. Rev. B* **2009**, *80*, 214417.
(62) Menyuk, N.; Dwight, K.; Wold, A. *J. Phys. (Paris)* **1964**, *25*, 528−536.
(63) Dutta, D. P.; Manjanna, J.; Tyagi, A. K. *J. Appl. Phys.* **2009**, *106*, 043915.
(64) Lawes, G.; Melot, B.; Page, K.; Ederer, C.; Hayward, M. A.; Proffen, T.; Seshadri, R. *Phys. Rev. B* **2006**, *74*, 024413.